SHIP DETECTION IN TERRASAR-X HIGH-RESOLUTION SPOTLIGHT DUAL-POLARISATION IMAGERY

Ken Yoong LEE and Timo Rolf BRETSCHNEIDER

EADS Innovation Works South Asia

110 Seletar Aerospace View, Singapore 797562
Tel: +65 65927324; Fax. +65 66591276
E-mail: {ken-yoong.lee, timo.bretschneider}@eads.net

KEY WORDS: TerraSAR-X, ship detection, global thresholding, squared radius, complex multivariate Gaussian distribution

Abstract: This paper addresses ship detection in TerraSAR-X single-look high-resolution spotlight data by using a global thresholding approach, which is based on statistical analysis of the test data. The corresponding thresholds were determined separately from the exponential and chi-squared distributions for TerraSAR-X single-polarisation (HH or VV) and dual-polarisation (HH and VV) data. From the results, all ship targets were successfully detected for different inputs, namely HH polarisation, VV polarisation, and dual-polarisation. The use of the dual-polarisation input was found to provide slightly better detection results of ship targets compared with the single-polarisation inputs. The visibility and detection of a small boat in the TerraSAR-X high-resolution spotlight data are also discussed in this paper.

1. INTRODUCTION

To date, the application of remotely sensed data, in particular with the use of synthetic aperture radar (SAR), for ship detection has been extensively studied (Benelli *et al*. 1994, Eldhuset 1996, Lombardo and Sciotti 2001, Yeremy *et al*. 2001). This is because the active radar imaging system is independent of daytime and weather conditions, which can then be used in the context of near real-time maritime security monitoring. Moreover, the wider coverage of spaceborne SAR data is also available through ScanSAR imaging mode, which allows the application to large-area coastal surveillance. A comprehensive review on ship detection from SAR imagery can be found in Crisp (2004).

The successful launch of TerraSAR-X has provided plentiful opportunities to examine the application of high-resolution dual-polarisation spaceborne data, especially through the spotlight imaging mode. Currently, there is a growing interest within the remote sensing community to utilise the acquired data for various applications. One of these potential applications is ship detection for maritime security and coastal surveillance. Among some recent research papers on this topic are Gabban *et al*. (2008), Paes *et al*. (2010), and Brusch *et al*. (2011).

In general, ship detection involves four main steps: 1) land masking, 2) pre-processing, 3) prescreening, and 4) discrimination. The first step is to mask out land areas since only ships in the water are of interest. Moreover, this can help to reduce false alarms caused by land cover features. In the second step, image enhancement is carried out, which is optional provided that a constant false alarm rate detector is employed for the subsequent prescreening. Then, the prescreening step, which is the most crucial step, identifies potential ship pixels in the masked input image. The final step, i.e. discrimination, is to reduce the false alarm rate. For instance, the observation of a ship wake can be employed to confirm the presence of a moving ship.

In the literature numerous prescreening algorithms have been proposed for the third step. These can be generally grouped into two categories, namely global and local processing approaches. In the former, an image pixel is marked as a potential ship pixel if its intensity or test statistic is greater than a predefined global threshold. For example, Lin *et al*. (1997) and Liu *et al*. (2005) applied this approach for ship detection in ERS SAR PRI and CV-580 SAR images, respectively. A careful threshold selection is prerequisite to successful ship detection by using this approach. For the latter, a local processing window is normally required. As shown in Figure 1, the processing window consists of a test pixel, which is surrounded by a guard ring and then by a background ring. The design of the guard ring is to exclude a possible extended ship target from a background ring and, hence, the background ring contains purely sea clutter. Local processing approaches have received a great deal of attention in ship detection (Casasent *et al*. 1999, Zhang and Wu 2008, Allard *et al*. 2009). However, the restriction with these approaches, in particularly for very high-resolution SAR data, is that the window size needs to be varied accordingly with different sizes of ship targets in order to enable an efficient detection.

In this paper, focus is placed on the crucial third step, i.e. prescreening of ship pixels in TerraSAR-X single-look dual-polarisation high-resolution spotlight data. The prescreening is performed through a global thresholding approach, where the threshold is determined from the statistical distribution of the test data. The details of the

TerraSAR-X test data are described in Section 2. Sections 3 and 4 present separately the ship detection in TerraSAR-X single-polarisation and dual-polarisation data. Finally, conclusions are given in Section 5.

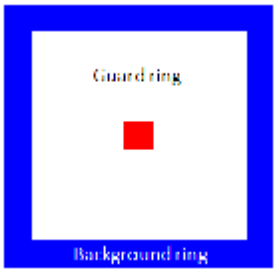

Figure 1. Typical window design, which is used by local prescreening algorithms.

2. DATA ACQUISITION

In TerraSAR-X single-look slant-range dual-polarisation (HH and VV polarisations) spotlight data, each pixel can be represented by a two-dimensional complex vector as

$$\mathbf{s} = \begin{bmatrix} s_{\mathrm{HH}} \\ s_{\mathrm{VV}} \end{bmatrix} = \begin{bmatrix} \Re(s_{\mathrm{HH}}) + i\Im(s_{\mathrm{HH}}) \\ \Re(s_{\mathrm{VV}}) + i\Im(s_{\mathrm{VV}}) \end{bmatrix}, \tag{1}$$

where $i = \sqrt{-1}$. The symbols $\Re(.)$ and $\Im(.)$ denote the real and imaginary parts of the backscattered complex signal s, respectively. The signed 16-bit real and imaginary values are calibrated by multiplying with the square root of the calibration factor provided in the annotation file (Fritz 2007). The radar brightness or beta naught, which is defined as the average radar cross section per unit pixel area, can be computed by taking the modulus, i.e. the sum of square of both the calibrated real and imaginary components. To simplify the development of a ship target detector in this study, the complex vector $\mathbf{s}$ of a homogeneous area (i.e. sea clutter) is assumed to be independent and identically distributed as a zero-mean bivariate complex Gaussian

$$f(\mathbf{s}) = \pi^{-2} |\boldsymbol{\Sigma}|^{-1} \exp\left(-\mathbf{s}^{*T} \boldsymbol{\Sigma}^{-1} \mathbf{s}\right), \tag{2}$$

where $\boldsymbol{\Sigma}$ is the population covariance matrix. The symbols $*$ and T denote the complex conjugate and transpose, respectively. The notation $|\,.\,|$ refers to the matrix determinant. The population squared radius $2\mathbf{s}^{*T}\boldsymbol{\Sigma}^{-1}\mathbf{s}$ follows a chi-squared distribution with four degrees of freedom. The proof can be obtained (see Appendix A) through expressing the above bivariate complex Gaussian distribution as four-dimensional real Gaussian distribution, followed by the use of the Mahalanobis transformation. In most cases the population covariance matrix remains unknown. This parameter can, however, be estimated from the samples based on the maximum likelihood method. As proven in Appendix B, the exact distribution of the sample squared radius is a beta distribution. It depends merely on the vector dimension and the number of samples N. For a large value of N (e.g. >1000), it is nevertheless acceptable to use the population squared radius instead in designing a ship target detector, which is discussed further in Section 4.

Three sets of TerraSAR-X single-look high-resolution spotlight data were provided by Astrium GEO-information Services for this study. The TerraSAR-X data with HH and VV polarizations were acquired separately on 11th of May 2011, 5th of August 2011, and 7th of August 2011. Note that only the derived results from the TerraSAR-X data, which were acquired on 5th of August 2011, are reported in this paper. Covering a coastal area of Tuas in Singapore, the resolution of the test data is 1.779 m in ground range and 2.2 m in azimuth. Figure 2 presents the TerraSAR-X test scene, where the incidence angle is 41.38°. The coordinates of the scene centre are E103°35'15" and N01°13'54". During the TerraSAR-X data acquisition, field work was conducted concurrently for collecting Automatic Identification System (AIS) data. In Figure 2, the extracted ship names and category types from the collected AIS information are overlaid on the acquired TerraSAR-X scene. It was found that there were five main different types of ship targets, namely cargo ships, dredger, explorers, tankers, and tugs. Figure 3 presents selected photos of several ships, which were identified during the field work. Two oil rigs were also noticed with the corresponding photos shown in Figures 3(e) and (f).

3. SHIP DETECTION IN TERRASAR-X SINGLE-POLARISATION DATA

To detect ship targets in TerraSAR-X single-polarisation data, a direct statistical modelling of ship targets is ideally preferred. However, the modelling is challenging and complicated due to different ship types and structures. Thus, in this study, sea clutter was chosen instead of ship targets in order to describe the opposite. As shown in Figure 2, a training area comprising 673460 pixels was identified for sea clutter modelling. The histograms of the real and imaginary components as well as radar brightness were then constructed individually from the selected training area

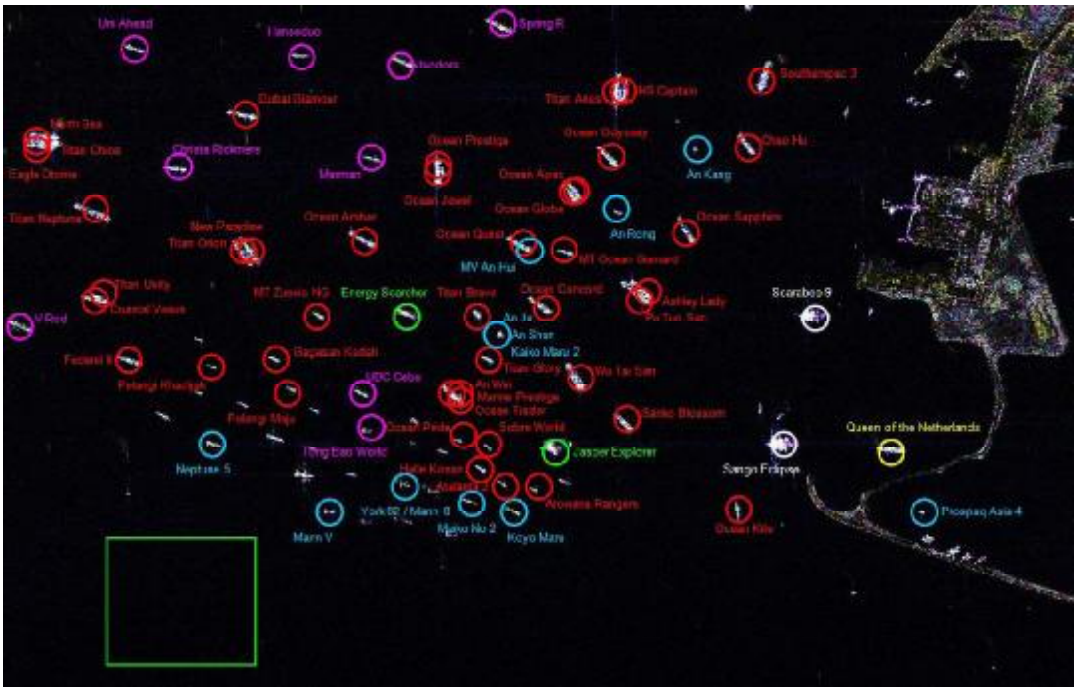

Figure 2. TerraSAR-X single-look slant-range dual-polarisation scene acquired on 5th of August 2011 around 7.20 pm (GMT+8). The TerraSAR-X satellite pass direction is ascending with its imaging direction to the right. In this figure, $|s_{HH}|^2$, $|s_{VV}|^2$, and $|s_{HH} - s_{VV}|^2$ are displayed in red, green, and blue (RGB) colour space. The green square is the training area of sea clutter identified in this study. The ground truth information is overlaid on the TerraSAR-X scene, where cargo ships, dredger, explorers, tankers, tugs, and oil rigs are circled in magenta, yellow, green, red, cyan, and white, respectively.

(a) (b) (c)

(d) (e) (f)

Figure 3. Photos captured during the field work. The tanker in (a) is Wu Tai San (MMSI: 563359000, length: 333 m, width: 60 m). (b) shows the picture of Sanko Blossom (MMSI: 371361000, length: 239 m, width 42 m). In (c), the tanker on port is Pu Tuo San (MMSI: 566079000, length 333 m, width: 60 m) while the one on starboard is Ashley Lady (MMSI: 565712000, length: 247 m, width: 32 m). The photo of Jasper Explorer (MMSI: 564347000, length: 165 m, width: 30 m) is shown in (d). Oil rigs in (e) and (f) are Scarabeo 9 (MMSI: 311046800) and Songa Eclipse (MMSI: 538004130), respectively.

of sea clutter. For both the real and imaginary components, the probability density function (pdf) of Gaussian distribution was superimposed on the constructed histograms and can be expressed as

$$f(x) = \frac{1}{\sqrt{2\pi}\sigma} \exp\left(-\frac{(x-\mu)^2}{2\sigma^2} \right), \quad (3)$$

where x refers to the random real (or imaginary) component. The parameters μ and σ are the mean and standard deviation, which are estimated by using all pixels in the selected training area. For the radar brightness, the constructed histograms were fitted with the exponential distribution

$$f(y) = \frac{1}{\theta}\exp\left(-\frac{y}{\theta}\right), \tag{4}$$

where y is the random radar brightness value. The scale parameter θ is also estimated by using all pixels in the training area. Figure 4 shows the histograms constructed from the training area. For the real and imaginary components of both the HH and VV polarisations, it is as expected that the Gaussian distribution fitted well, while the exponential distribution was found to be well-fitted for the radar brightness.

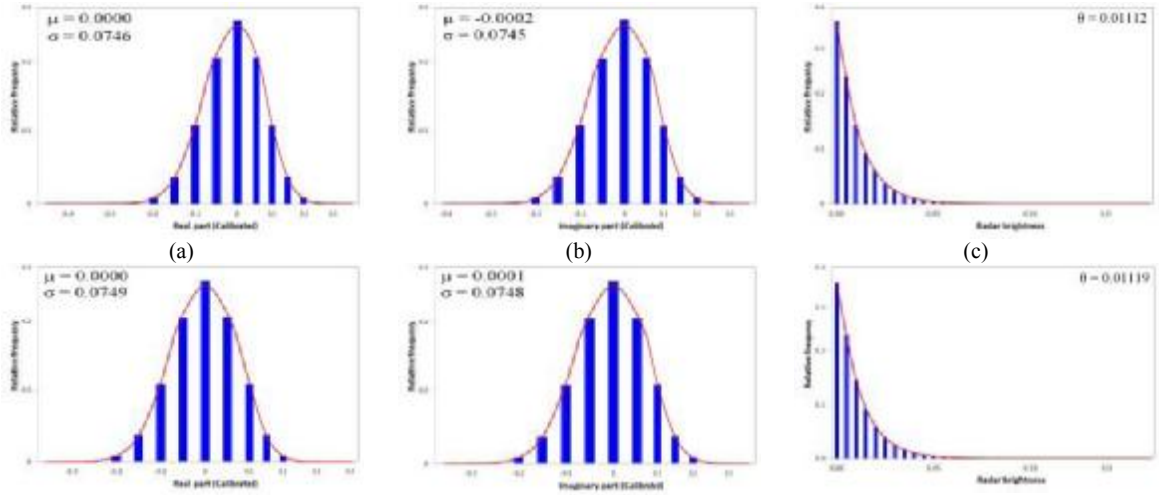

Figure 4. Histograms constructed from selected training area of sea clutter. (a) real component of HH polarisation, (b) imaginary component of HH polarisation, (c) radar brightness of HH polarisation, (d) real component of VV polarisation, (e) imaginary component of VV polarisation, and (f) radar brightness of VV polarisation. Note that the fitted probability density function is plotted in red colour.

For detecting potential ship targets in TerraSAR-X radar brightness data, the upper bound critical value t is firstly determined from the fitted exponential distribution with a user-specified significance level. Note that the significance level α is also known as probability of false alarm in other words. In mathematical form, it is given below:

$$\alpha = 1 - \int_0^t f(y)\,dy. \tag{5}$$

A test pixel is marked as a ship pixel if its radar brightness value is greater than the critical value, which is employed as a threshold. Figures 5(a) and (b) show separately selected ship detection results for the HH and VV polarisations. The thresholds (or critical values) were determined by using the fitted exponential distribution with a significance level of 1×10^{-10}, where the values were 0.25612 and 0.25777 for both the HH and VV polarisations, respectively. From the obtained results, all ship targets were found to be properly detected in both the HH and VV polarisations. These promising results might be due to the use of the TerraSAR-X high-resolution spotlight imaging mode. Each ship target in the TerraSAR-X high-resolution spotlight data was found to contain many bright pixels and exhibits a very distinct contrast against the background of sea clutter, rather than to present itself in form of a single ambiguous pixel or just several pixels. In addition, it was noticed during the field work that the sea was relatively calm over the test area, where the wind speed was about 2m/s. Consequently, the sea surface appeared relatively homogeneous and was easier to be statistically modelled in the captured TerraSAR-X scene. In Figure 5(a), two false alarms can, however, be clearly observed. Both the two oil rigs (as circled in magenta) were mistakenly detected as ship targets owing to their ship-like strong backscattering characteristics.

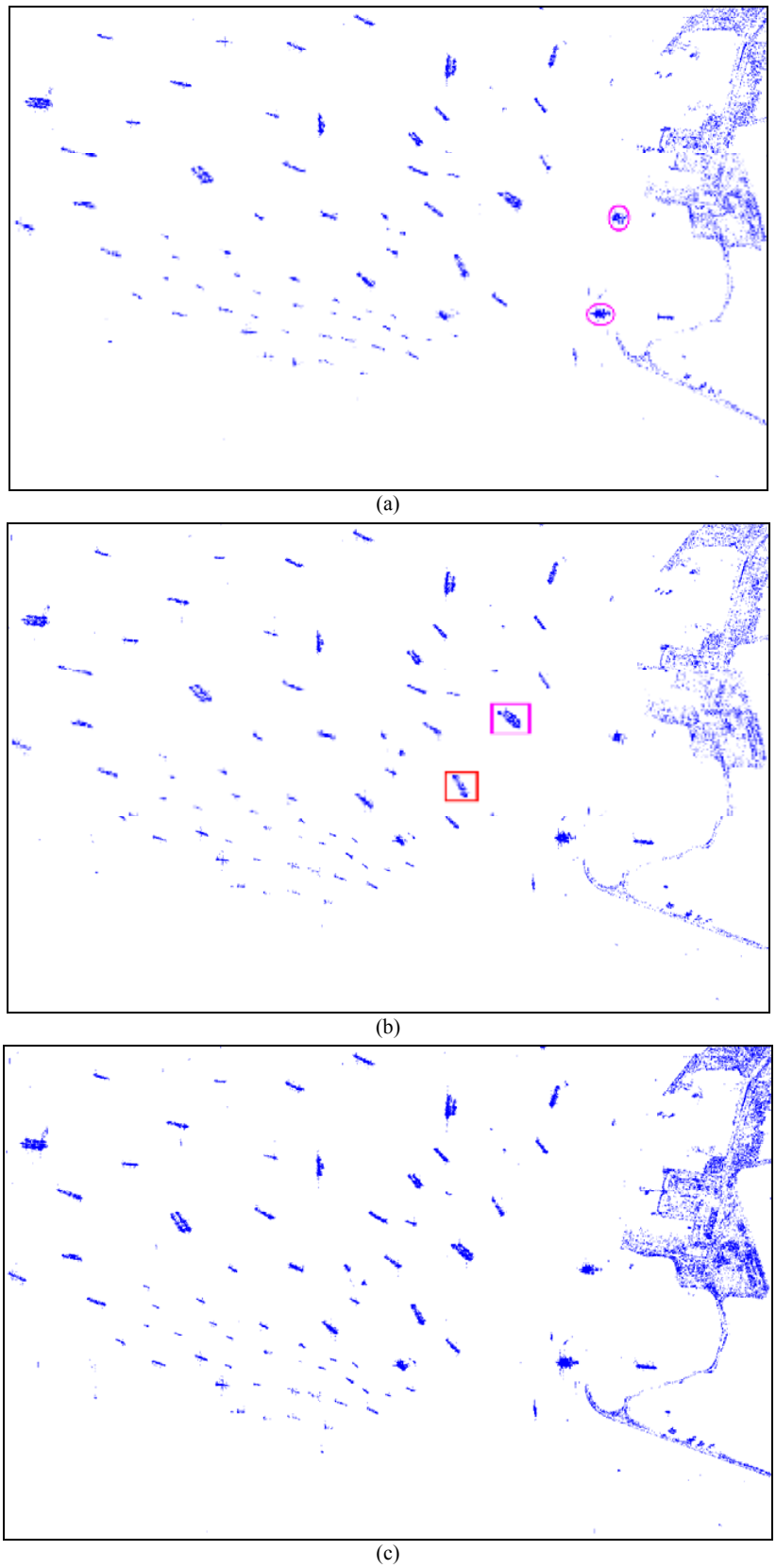

(a)

(b)

(c)

Figure 5. Ship detection results from (a) HH polarisation, (b) VV polarisation, and (c) dual-polarisation. The detected ship targets are coloured in blue. Note that no land masking was performed. Hence, the reclaimed area of Tuas, Singapore was also detected and can be seen on the right-hand side.

4. SHIP DETECTION IN TERRASAR-X DUAL-POLARISATION DATA

For TerraSAR-X dual-polarisation data, ship detection is carried out based on the aforementioned population squared radius, i.e. $2\mathbf{s}^{*T}\boldsymbol{\Sigma}^{-1}\mathbf{s}$, which follows the chi-squared distribution with four degrees of freedom. The processing steps are outlined below:

1) Estimate the covariance matrix $\hat{\boldsymbol{\Sigma}}_{\text{sea}}$ from selected training area of sea clutter:

$$\hat{\boldsymbol{\Sigma}}_{\text{sea}} = \frac{1}{N}\sum_{i=1}^{N}\mathbf{s}_i\mathbf{s}_i^{*T}, \tag{6}$$

where $\mathbf{s}_i$ refers to the complex vector of a pixel i in the identified training area of sea clutter. The variable N denotes the total number of pixels in the training area.

2) Mark the test pixel j as a ship pixel if the following criterion is fulfilled:

$$2\mathbf{s}_j^{*T}\hat{\boldsymbol{\Sigma}}_{\text{sea}}^{-1}\mathbf{s}_j > t. \tag{7}$$

The upper bound critical value t is obtained from the chi-squared distribution with a desired significance level.

3) Move to next pixel and repeat Step 2. Terminate the execution if there are no more test pixels to be processed.

Figure 6 plots the histogram of population squared radius for the selected training area, where the computed covariance matrix of sea clutter is given below:

$$\hat{\boldsymbol{\Sigma}}_{\text{sea}} = \begin{bmatrix} 0.01112 & 0.00017+0.00007i \\ 0.00017-0.00007i & 0.01119 \end{bmatrix}.$$

Noticeably, the chi-squared distribution with four degrees of freedom was found to fit well. Figure 5(c) shows the ship detection result from TerraSAR-X dual-polarisation data. The threshold was set to 52.668 based on the chi-squared distribution with a significance level of 1×10^{-10}. An enlarged window containing two large tankers, namely Pu Tuo San and Ashley Lady, was extracted from Figure 5 and is presented in Figure 7. The photo of the two tankers can be viewed in Figure 3(c). By comparing Figures 7(b)–(d), it is apparent that both the tankers were better delineated by using the dual-polarisation input compared with the single-polarisation inputs. The same finding can be derived from Figure 8 for other tanker, i.e. Wu Tai San, where a better delineation was obtained by using the dual-polarisation input.

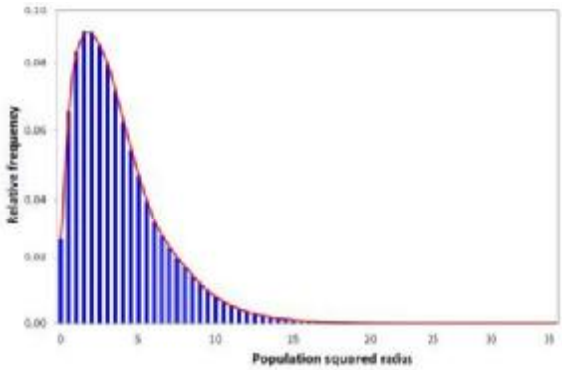

Figure 6. A histogram of population square radius constructed from selected training area of sea clutter. Note that the fitted probability density function of the chi-squared distribution (with four degrees of freedom) is plotted in red colour.

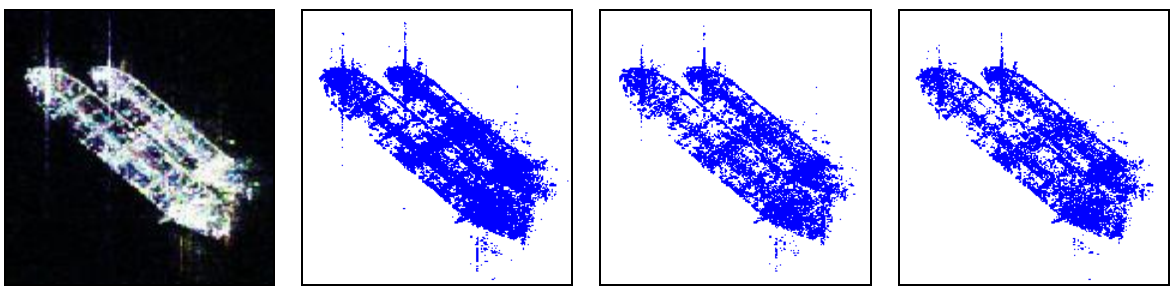

(a) (b) (c) (d)

Figure 7. An enlarged window containing two large tankers, namely Pu Tuo San and Ashley Lady. The location of the two tankers is indicated by a magenta square in Figure 5(b). In (a), the tanker on port is Pu Tuo San while Ashley Lady is on starboard, where $|s_{HH}|^2$, $|s_{VV}|^2$, and $|s_{HH} - s_{VV}|^2$ are displayed in RGB colour space. The detection results of dual-polarisation, HH polarisation, and VV polarisation based on a significance level of 1×10^{-10} are shown in (b), (c), and (d), respectively.

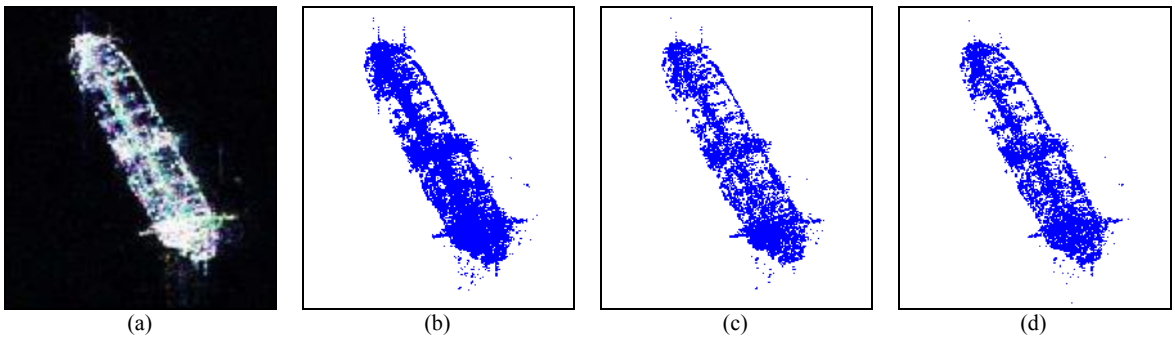

(a) (b) (c) (d)

Figure 8. An enlarged window containing one tanker, i.e. Wu Tai San. Its appearance in TerraSAR-X high-resolution spotlight data is given in (a), where $|s_{HH}|^2$, $|s_{VV}|^2$, and $|s_{HH} - s_{VV}|^2$ are displayed in RGB colour space. The location of the tanker is indicated by a red square in Figure 5(b), while the photo of the tanker can be found in Figure 3(a). The detection results of dual-polarisation, HH polarisation, and VV polarisation based on a significance level of 1×10^{-10} are shown in (b), (c), and (d), respectively.

Further comparison on the use of TerraSAR-X dual-polarisation and single-polarisation inputs, in particularly for detecting a small boat, was conducted. A seven-meter long survey boat was deployed during the TerraSAR-X data acquisition on 5th of August 2011. Figure 9(a) indicates the location of the survey boat in the captured TerraSAR-X scene. The survey boat was stationed near two large tankers, namely Wu Tai San and Sanko Blossom. A picture of the survey boat is given in Figure 9(b), while the photos of the two tankers can be found in Figure 3. Note that the survey boat is mainly made from fibreglass and metal is only used for the handrail as well as the outboard engine. Figures 10(d)–(f) show the corresponding detection outputs of the survey boat, which were extracted from the results presented in Figure 5. It is evident that more pixels were detected for the survey boat by using the dual-polarisation input compared with only the single-polarisation input (HH or VV polarisation).

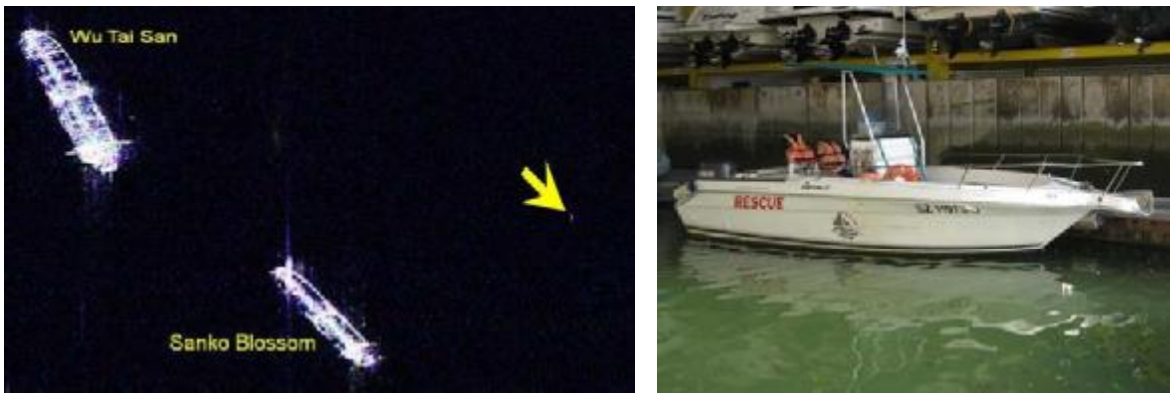

(a) (b)

Figure 9. Location and photo of survey boat, where the arrow in (a) indicates the location of the deployed survey boat in the TerraSAR-X test scene.

(a) (b) (c) (d) (e) (f)

Figure 10. Detection of survey boat in TerraSAR-X single-look high-resolution spotlight data. The picture of the survey boat is provided in Figure 9(b). Its appearance in HH, VV, and dual-polarisation are given in (a), (b), and (c). In (c), $|s_{HH}|^2$, $|s_{VV}|^2$, and $|s_{HH} - s_{VV}|^2$ are displayed in RGB colour space. The detection results from HH, VV, and dual-polarisation based on a significance level of 1×10^{-10} are shown separately in (d), (e), and (f).

5. CONCLUSIONS AND RECOMMENDATION

In this paper, ship detection in TerraSAR-X single-look high-resolution spotlight data was presented, where no additional speckle filtering was applied to the test data prior to the detection. To detect ship targets, a global thresholding approach was adopted. The thresholds were determined separately from the exponential and chi-squared distributions for both the single-polarisation (HH or VV polarisation) and dual-polarisation (HH and VV polarisations) data. The merit of this approach is that no selection of window size is required. Thus, both smaller and larger ships can be detected in the same processing step simultaneously. In this study, the use of the dual-polarisation input was found to provide slightly better detection results of ship targets compared with the single-polarisation inputs. False detections did, however, occur due to the presence of two oil rigs in the scene. Finally, the visibility and detection of the deployed survey boat in the TerraSAR-X high-resolution spotlight data were also investigated and confirmed. The experimental results showed that more pixels were detected for the small boat by using the dual-polarisation input compared with only individual single-polarisation input (HH or VV polarisation). Further work can be conducted by considering ship detection in TerraSAR-X spotlight data in rougher sea conditions.

APPENDICES

A. Population Squared Radius Follows a Chi-Squared Distribution

Theorem 1: If $\mathbf{s}$ is a p-dimensional zero-mean complex Gaussian vector, the probability density function of $\mathbf{s}$ is given in Andersen *et al*. (1995) by

$$f(\mathbf{s}) = \pi^{-p}\left|\boldsymbol{\Sigma}_{\mathrm{c}}\right|^{-1}\exp\left(-\mathbf{s}^{*T}\boldsymbol{\Sigma}_{\mathrm{c}}^{-1}\mathbf{s}\right), \tag{8}$$

where $\boldsymbol{\Sigma}_{\mathrm{c}}$ is a $p\times p$ dimensional positive definite Hermitian covariance matrix. The complex vector $\mathbf{s}$ can also be written in form of a $2p$-dimensional real vector as

$$\mathbf{x} = \left[\Re(s_1) \quad \Im(s_1) \quad \ldots \quad \Re(s_p) \quad \Im(s_p)\right]^T. \tag{9}$$

The probability density function of $\mathbf{x}$ is

$$f(\mathbf{x}) = (2\pi)^{-2p/2}\left|\boldsymbol{\Sigma}_{\mathrm{r}}\right|^{-1/2}\exp\left(-\tfrac{1}{2}\mathbf{x}^T\boldsymbol{\Sigma}_{\mathrm{r}}^{-1}\mathbf{x}\right), \tag{10}$$

where $\boldsymbol{\Sigma}_{\mathrm{r}}$ is a $2p\times 2p$ dimensional positive definite real symmetric covariance matrix (Andersen *et al*. 1995, p. 26; Hagedorn *et al*. 2006, p. 658). The population squared radius $\mathbf{x}^T\boldsymbol{\Sigma}_{\mathrm{r}}^{-1}\mathbf{x}$, which is also equal to $2\mathbf{s}^{*T}\boldsymbol{\Sigma}_{\mathrm{c}}^{-1}\mathbf{s}$, follows a chi-squared distribution with $2p$ degrees of freedom.

Proof: Let $\mathbf{y} = \boldsymbol{\Sigma}_{\mathrm{r}}^{-1/2}\mathbf{x}$, which is also called Mahalanobis transformation (Härdle and Simar 2007, p. 108; Härdle and Hlávka, p. 56), then the inverse linear transformation is

$$\mathbf{x} = \boldsymbol{\Sigma}_{\mathrm{r}}^{1/2}\mathbf{y} \tag{11}$$

and the Jacobian matrix of the transformation $\mathbf{y}$ going to $\mathbf{x}$ is

$$\mathbf{J} = \boldsymbol{\Sigma}_{\mathrm{r}}^{1/2}. \tag{12}$$

Hence, the probability density function of $\mathbf{y}$ is given by

$$f(\mathbf{y}) = \left|\boldsymbol{\Sigma}_{\mathrm{r}}^{1/2}\right|(2\pi)^{-2p/2}\left|\boldsymbol{\Sigma}_{\mathrm{r}}\right|^{-1/2}\exp\left\{-\tfrac{1}{2}\left(\boldsymbol{\Sigma}_{\mathrm{r}}^{1/2}\mathbf{y}\right)^T\boldsymbol{\Sigma}_{\mathrm{r}}^{-1}\left(\boldsymbol{\Sigma}_{\mathrm{r}}^{1/2}\mathbf{y}\right)\right\}. \tag{13}$$

Since $\boldsymbol{\Sigma}_{\mathrm{r}}$ is a positive definite matrix, its eigenvalues λ are always positive. Thus,

$$\left|\boldsymbol{\Sigma}_{\mathrm{r}}\right|^{-1/2} = \left(\sqrt{\lambda_1\cdot\lambda_2\cdot\ldots\cdot\lambda_{2p}}\right)^{-1}. \tag{14}$$

Similarly, the eigenvalues of $\boldsymbol{\Sigma}_{\mathrm{r}}^{1/2}$ are also positive, i.e. $\sqrt{\lambda_1}$, …, $\sqrt{\lambda_{2p}}$. Hence,

$$\left|\boldsymbol{\Sigma}_{\mathrm{r}}^{1/2}\right| = \sqrt{\lambda_1\cdot\lambda_2\cdot\ldots\cdot\lambda_{2p}}. \tag{15}$$

Based on these facts, Equation (13) can be simplified as

$$f(\mathbf{y}) = (2\pi)^{-2p/2}\exp\left\{-\tfrac{1}{2}\left(\boldsymbol{\Sigma}_{\mathrm{r}}^{1/2}\mathbf{y}\right)^T\boldsymbol{\Sigma}_{\mathrm{r}}^{-1}\left(\boldsymbol{\Sigma}_{\mathrm{r}}^{1/2}\mathbf{y}\right)\right\}. \tag{16}$$

Moreover, $\left(\boldsymbol{\Sigma}_{\mathrm{r}}^{1/2}\mathbf{y}\right)^T$ can be written as $\mathbf{y}^T\boldsymbol{\Sigma}_{\mathrm{r}}^{1/2}$. Subsequently,

$$f(\mathbf{y}) = (2\pi)^{-2p/2}\exp\left(-\tfrac{1}{2}\mathbf{y}^T\boldsymbol{\Sigma}_{\mathrm{r}}^{1/2}\boldsymbol{\Sigma}_{\mathrm{r}}^{-1}\boldsymbol{\Sigma}_{\mathrm{r}}^{1/2}\mathbf{y}\right) = (2\pi)^{-2p/2}\exp\left(-\tfrac{1}{2}\mathbf{y}^T\mathbf{y}\right). \tag{17}$$

From Equation (17), it is clearly seen that $\mathbf{y}$ follows a $2p$-variate standard Gaussian distribution, i.e. $N_{2p}(\mathbf{0}, \mathbf{I})$. The elements of $\mathbf{y}$ are independent random variables with standard univariate Gaussian distribution since the covariance matrix is an identity matrix. Keeping all these in mind,

$$\mathbf{x}^T \boldsymbol{\Sigma}_{\mathrm{r}}^{-1} \mathbf{x} = \mathbf{y}^T \mathbf{y} = \sum_{i=1}^{2p} y_i^2 \tag{18}$$

is a sum of squares of independent random variables with standard univariate Gaussian distribution. Therefore, the squared radius $\mathbf{x}^T \boldsymbol{\Sigma}_{\mathrm{r}}^{-1} \mathbf{x}$ has a chi-squared distribution with $2p$ degrees of freedom.

(Q.E.D)

B. Sample Squared Radius Follows a Beta Distribution

Lemma 1: Let $\mathbf{U}$ and $\mathbf{V}$ be $p \times p$ complex random matrices having central complex Wishart distributions, namely $CW_p(n, \boldsymbol{\Sigma})$ and $CW_p(1, \boldsymbol{\Sigma})$, respectively. If $\mathbf{U}$ and $\mathbf{V}$ are independent and $n \geq p$, then $|\mathbf{U}| / |\mathbf{U} + \mathbf{V}|$ has a beta distribution, i.e. beta$(n - p + 1, p)$.
The proof is given in Andersen *et al*. (1995, pp. 65–66).

Lemma 2: Let x have a beta distribution, i.e. beta(a, b). Then, the distribution of $1 - x$ is beta(b, a).
The proof is straightforward and omitted here.

Theorem 2: Let $\mathbf{s}_1, \mathbf{s}_2, \ldots, \mathbf{s}_N$ be independent and identically distributed as p-dimensional zero-mean complex Gaussian, i.e. $CN_p(\mathbf{0}, \boldsymbol{\Sigma})$. Then, $N^{-1} \mathbf{s}_i^{*T} \mathbf{C}^{-1} \mathbf{s}_i$ is distributed as beta$(p, N - p)$, where the sample covariance matrix $\mathbf{C} = N^{-1} \sum_{k=1}^{N} \mathbf{s}_k \mathbf{s}_k^{*T}$ is the maximum likelihood estimator of $\boldsymbol{\Sigma}$ (Goodman 1963, pp. 160–161).

Proof: Let $\mathbf{U} = \sum_{k=1, k \neq i}^{N-1} \mathbf{s}_k \mathbf{s}_k^{*T} \sim CW_p(N - 1, \boldsymbol{\Sigma})$ and $\mathbf{V} = \mathbf{s}_i \mathbf{s}_i^{*T} \sim CW_p(1, \boldsymbol{\Sigma})$. Both the matrices $\mathbf{U}$ and $\mathbf{V}$ are independent since $\mathbf{U}$ does not include $\mathbf{s}_i$. From Lemma 1, it is known that $|\mathbf{U}| / |\mathbf{U} + \mathbf{V}|$ has a beta distribution, i.e. beta$(N - p, p)$. Now, let

$$\mathbf{W} = \sum_{k=1}^{N} \mathbf{s}_k \mathbf{s}_k^{*T} = \mathbf{U} + \mathbf{V} = N\mathbf{C}, \tag{19}$$

then

$$\frac{|\mathbf{U}|}{|\mathbf{U} + \mathbf{V}|} = \frac{|\mathbf{W} - \mathbf{V}|}{|\mathbf{W}|} = 1 - \frac{1}{N} \mathbf{s}_i^{*T} \mathbf{C}^{-1} \mathbf{s}_i. \tag{20}$$

As a result,

$$1 - N^{-1} \mathbf{s}_i^{*T} \mathbf{C}^{-1} \mathbf{s}_i \sim \text{beta}(N - p, p). \tag{21}$$

Based on Lemma 2,

$$N^{-1} \mathbf{s}_i^{*T} \mathbf{C}^{-1} \mathbf{s}_i \sim \text{beta}(p, N - p). \tag{22}$$

(Q.E.D)

ACKNOWLEDGEMENT

The authors would like to express their gratitude to Astrium GEO-Information Services for providing the TerraSAR-X test datasets.

REFERENCES

Allard, Y., Germain, M., and Bonneau, O., 2009. Ship detection and characterization using polarimetric SAR data. In Shahbazian E., Rogova G., and DeWeert M.J. (Eds.), *Harbour Protection Through Data Fusion Technologies* (pp. 243–250). Dordrecht: Springer.

Andersen, H.H., Højbjerre, M., Sørensen, D., and Eriksen, P.S., 1995. Linear and graphical models for the multivariate complex normal distribution. *Lectures Notes on Statistics.* New York: Springer-Verlag.

Benelli, G., Garzelli, A., and Mecocci, A., 1994. Complete processing system that uses fuzzy logic for ship detection in SAR images. *IEE Proceedings of Radar, Sonar and Navigation*, 141(4), pp. 181–186.

Brusch, S., Lehner, S., Fritz, T., Soccorsi, M., Soloviev, A., and van Schie, B., 2011. Ship surveillance with TerraSAR-X. *IEEE Transactions on Geoscience and Remote Sensing*, 49(3), pp. 1092–1103.

Casasent, D., Su, W., Turaga, D., Narusawa, N., and Ashizawa, S., 1999. SAR ship detection using new conditional contrast box filter. *SPIE Proceedings*, vol. 3721, pp. 274–284.

Crisp, D.J., 2004. *The State-of-the-Art in Ship Detection in Synthetic Aperture Radar Imagery.* DSTO Information Sciences Laboratory: Technical report.

Eldhuset, K., 1996. An automatic ship and ship wake detection system for spaceborne SAR images in coastal regions. *IEEE Transactions on Geoscience and Remote Sensing*, 34(4), pp. 1010–1019.

Fritz, T., 2007. *Level 1b Product Format Specification.* DLR document no. TX-GS-DD-3307 (Issue 1.3).

Gabban, A., Greidanus, H., Smith, A.J.E., Anitori, L., Thoorens, F.-X., and Mallorqui, J., 2008. Ship surveillance with TerraSAR-X ScanSAR. Available online at http://sss.terrasar-x.dlr.de/papers_sci_meet_3/paper/OCE0105_gabban.pdf

Goodman, N.R., 1963. Statistical analysis based on a certain multivariate complex Gaussian distribution (an introduction). *The Annals of Mathematical Statistics*, 34(1), pp. 152–177.

Hagedorn, M., Smith, P.J., Bones, P.J., Millane, R.P., and Pairman, D., 2006. A trivariate chi-squared distribution derived from the complex Wishart distribution. *Journal of Multivariate Analysis*, 97(3), pp. 655–674.

Härdle, W. and Hlávka, Z., 2007. *Multivariate Statistics: Exercises and Solutions*. New York: Springer.

Härdle, W. and Simar, L., 2007. *Applied Multivariate Statistical Analysis.* Berlin: Springer.

Lin, I-I, Kwoh, L.K., Lin, Y.-C., and Khoo, V., 1997. Ship and ship wake detection in the ERS SAR imagery using computer-based algorithm. *Proceedings of IEEE International Geoscience and Remote Sensing Symposium*, vol. 1, pp. 151–153.

Liu, C., Vachon, P.W., and Geling, G.W., 2005. Improved ship detection with airborne polarimetric SAR data. *Canadian Journal of Remote Sensing*, 31(1), pp. 122–131.

Lombardo, P. and Sciotti, M., 2001. Segmentation-based techniques for ship detection in SAR images. *IEE Proceedings of Radar, Sonar and Navigation*, 148(3), pp. 147–159.

Paes, R.L., Lorenzzetti, J.A., and Gherardi, D.F.M., 2010. Ship detection using TerraSAR-X images in the Campos Basin (Brazil). *IEEE Geoscience and Remote Sensing Letters*, 7(3), pp. 545–548.

Yeremy, M., Campbell, J.W.M., Mattar, K., and Potter, T., 2001. Ocean surveillance with polarimetric SAR. *Canadian Journal of Remote Sensing*, 27(4), pp. 328–344.

Zhang, F. and Wu, B., 2008. A scheme for ship detection in inhomogeneous regions based on segmentation of SAR images. *International Journal of Remote Sensing*, 29(19), pp. 5733–5747.